NUCL SCI TECH (2019) 30:184
https://doi.org/10.1007/s41365-019-0699-7

Transverse emittance measurement for the heavy ion medical machine cyclotron

Yong-Chun Feng[1,2] · Min Li[1] · Rui-Shi Mao[1] · Bing Wang[1] · Sheng-Peng Li[3] · Wei-Long Li[1,2] · Wei-Nian Ma[1] · Xin-Cai Kang[1,4] · Jin-Quan Zhang[1] · Peng Li[1] · Tie-Cheng Zhao[1] · Zhi-Guo Xu[1] · You-Jin Yuan[1]

Received: 4 March 2019 / Revised: 11 July 2019 / Accepted: 13 July 2019 / Published online: 22 November 2019

Abstract The transverse emittance of the extracted beam from the heavy ion medical machine cyclotron is measured and then optimized for injection into the synchrotron. For the purposes of cross-validation, three methods, i.e., slit–grid, Q-scan, and 3-grid, are used to measure the emittance. In the slit–grid technique, an automatic selection of the region of interest is adopted to isolate the major noise from the beam phase space, which is an improvement over the traditional technique. After iterating over the contour level, an unbiased measurement of the emittance can be obtained. An improvement in the thin lens technique is implemented in the Q-scan method. The results of these measurements are presented.

Keywords Heavy ion medical machine · Transverse emittance · Slit–grid

This work was supported by the National Natural Science Foundation of China (No. 11775281)

✉ Rui-Shi Mao
maorsh@impcas.ac.cn

1 Institute of Modern Physics, Chinese Academy of Sciences, Lanzhou 730000, China

2 School of Nuclear Science and Technology, University of Chinese Academy of Sciences, Beijing 100049, China

3 Lanzhou Ke jin tai ji Corporation, LTD, Lanzhou 730000, China

4 Lanzhou University of Technology, Lanzhou 730050, China

1 Introduction

The heavy ion medical machine (HIMM) developed by the Institute of Modern Physics is now undergoing a clinical trial [1, 2]. It consists of two electron cyclotron resonance (ECR) ion sources, a cyclotron, and a synchrotron that has a compact structure with a circumference of 56.2 m. The feedback-based slow-extraction technique [3] is adopted to deliver a high-quality beam spill into five treatment terminals. The layout of the HIMM complex is shown in Fig. 1. The cyclotron is critical for optimized injection into the synchrotron. The HIMM cyclotron is an isochronous machine with four magnet sectors and two RF-gap Dees that accelerate $^{12}C^{5+}$ to approximately 7 MeV/u. The extracted beam intensity is up to 10 μA in continuous wave (CW) mode. Preliminary calculations indicate that the emittance containing 95% of beam particles is up to 60 mm mrad. Up to now, the slow-extraction efficiency has reached nearly 90% for all energies from 120 to 400 MeV/u. The spill duty factor has exceeded 90% at a sample rate of 10 kHz [4].

Emittance is one of the critical beam parameters for accelerators that reveal the beam quality directly. The definitions of phase space and emittance are well documented in Refs. [5, 6]. The most commonly used methods to extract the emittance include the slit–grid [7, 8], pepper-pot [9–11], Quadrupole-scan (Q-scan) [12–14], and 3-grid [13, 15] techniques. During the commissioning phase of a newly designed machine, the slit–grid and pepper-pot techniques are the standard methods used to display the intensity distribution of a phase space with an arbitrary shape. Aberrations and filamentation induced by mismatch, higher-order effects of the beam optics as well as space-charge effects can then be investigated in a straightforward

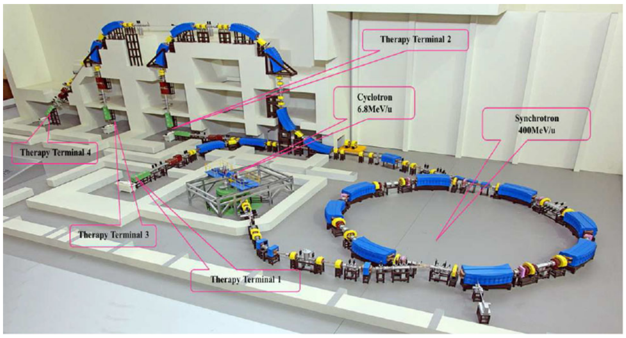

Fig. 1 Layout of the HIMM complex

manner [16]. However, the pepper-pot must be calibrated very carefully using extremely parallel light before a reliable result is obtained, so we do not make use of this method in this study.

Before integrating the cyclotron into the HIMM complex, a dedicated beam line has been constructed temporarily at the Institute of Modern Physics (IMP), and the emittance measurements are taken along it. In this paper, the measurements of the transverse emittance using the three methods mentioned above are discussed, and the automatic selection technique of the Region Of Interest (ROI) is described in detail.

2 Experimental setup

The diagnostics beam line is located at the exit of the cyclotron, as shown in Fig. 2. Two pairs of slits (SL) are employed to perform the slit–grid measurement. Four multi-wire (MW) monitors are used to sample the beam profile and also perform the 3-grid measurement. The distance between these devices is calibrated using a FARO Laser Tracker, and the position coordinates are summarized in Table 1. Each MW has a sensitive area of 47 mm $\times$ 47 mm, which corresponds to 47 wires for both the horizontal and vertical directions with a gap of 1 mm and a diameter of 0.2 mm. The readouts for the x and y directions are separate, so the measurement can be taken for both planes simultaneously. Each pair of slits scans the beam for its corresponding plane. Both of the slits are driven by a servo motor with positioning precision better than 1 μm. Along the beam line, two Faraday cups (FCs) are installed. FC1 is located before the entrance of MW1, and FC2 is at the end of the beam line. Both of the FCs can be used to measure beam intensity. FC2, however, acts as the beam dump and is, therefore, always kept inside the beam line. FC1 is used to block the beam, while the MW is pushed into the beam pipe center, which can protect the MW electronics against radiation damage. During the measurement, it is removed from the beam line.

To reduce the thermal loading of the MW, a chopper upstream of the cyclotron is powered on during the emittance measurement, which decreases the CW current to 1 μA. The data acquisition system is based on NI's CompactRIO controller, which runs on a real-time system with a reaction time of less than 1 ms and has a fast calculation ability [17]. A LabVIEW-based routine is developed to control the motion of the motors and acquire MW profile information. The collected data are first stored on disk, and then, a Python-based post-processing script is employed for further analysis. The data length is determined by the sample time, and the average thereof over the total data gives a more reliable measurement.

Fig. 2 Beam diagnostics layout

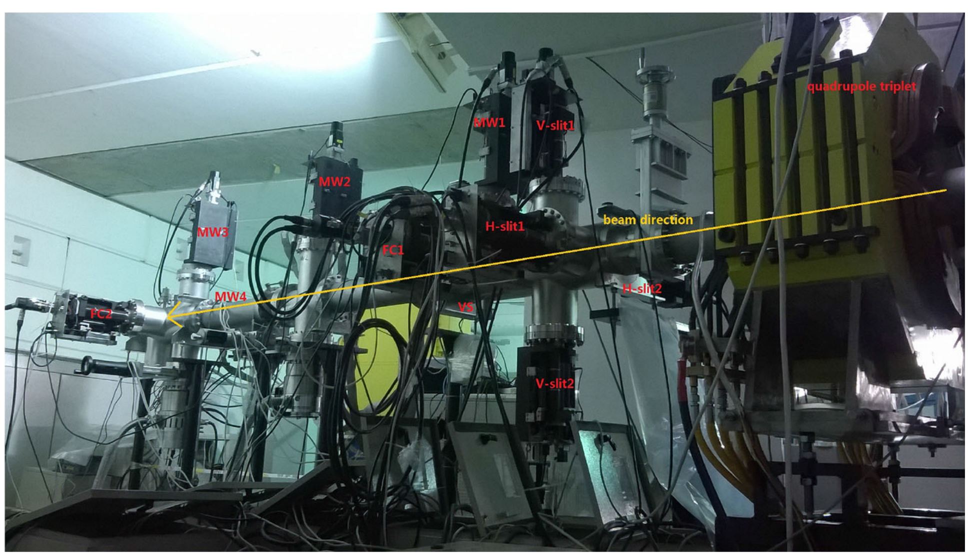

Table 1 Position coordinates of the slits and MWs

Device	SL1/SL2	SL3/SL4	MW1	MW2	MW3	MW4
Position (mm)	2451.2	2611.4	2929.85	4001.1	5123.6	5280.7

3 Emittance measurement

3.1 Slit–grid technique

In a low-energy heavy ion machine, the slit–grid technique is one of the most widely used methods for emittance diagnostics. In this method, a small slit opening selects the beamlet at that position, and an MW located downstream samples the distribution and reveals the divergence of the beamlet. By scanning the slit across the beam cross section, the whole phase space can be obtained, which generates a two-dimensional (2D) data matrix that is just the area used in the emittance calculation. Thus, the emittance can be retrieved statistically according to the algorithm given in Ref. [18].

$$
\begin{aligned}
&\mathrm{Sum} = \sum_{n_x}\sum_{n_{x\prime}} I_{n_x,n_{x\prime}}\\
&X_0 = \frac{1}{\mathrm{Sum}}\sum_{n_x}\sum_{n_{x\prime}} n_x I_{n_x,n_{x\prime}}\\
&X_{0\prime} = \frac{1}{\mathrm{Sum}}\sum_{n_x}\sum_{n_{x\prime}} n_{x\prime} I_{n_x,n_{x\prime}}\\
&D_x = \frac{\Delta_{x^2}}{\mathrm{Sum}}\sum_{n_x}\sum_{n_{x\prime}} [n_x - X_0]^2 I_{n_x,n_{x\prime}}\\
&D_{x\prime} = \frac{\Delta_{x\prime^2}}{\mathrm{Sum}}\sum_{n_x}\sum_{n_{x\prime}} [n_{x\prime} - X_0']^2 I_{n_x,n_{x\prime}}\\
&M_{xx\prime} = \frac{\Delta x\Delta_{x'}}{\mathrm{Sum}}\sum_{n_x}\sum_{n_{x\prime}} [n_x - X_0]^2[n_{x\prime} - X_0'] I_{n_x,n_{x\prime}}\\
&\sigma_x = \sqrt{D_x},\quad \sigma_{x\prime} = \sqrt{D_{x\prime}},\quad \rho = \frac{M_{xx\prime}}{\sigma_x\sigma_{x\prime}}
\end{aligned}
\tag{1}
$$

In this way, the root mean square (RMS) emittance and TWISS parameters can be evaluated by

$$
\begin{aligned}
&\varepsilon_x = \sigma_x\sigma_{x'}\sqrt{1-\rho^2}\\
&\beta = \frac{\sigma_x}{\sigma_{x'}}\frac{1}{\sqrt{1-\rho^2}}\\
&\gamma = \frac{\sigma_{x'}}{\sigma_x}\frac{1}{\sqrt{1-\rho^2}}\\
&\alpha = -\rho\sqrt{\beta\gamma}
\end{aligned}
\tag{2}
$$

where $I_{n_x,n_{x'}}$ represents the entries of the data matrix and n_x and $n_{x'}$ are the total number of rows and columns, which correspond to the scan number and wire number, respectively. Area elements $\Delta x\Delta x'$ are determined by the step width of the slit and the gap of the MW and are defined by $\Delta x = (x_{\mathrm{max}} - x_{\mathrm{min}})/n_x$ and $\Delta x' = (x'_{\mathrm{max}} - x'_{\mathrm{min}})/n_{x'}$. X_0 and X_0' give the center of the matrix.

Typically, the data are noisy owing to disturbances from the MW electronics and the environment. It is, therefore, necessary to denoise the data before performing the calculation using Eq. 2. In this paper, we use a systematic procedure to complete the emittance evaluation. The three steps to perform the image denoising are discussed below.

3.1.1 *Interpolation*

An ad hoc-based interpolation is implemented along a specified axis, upon which the phase space distribution can be refined, and therefore, the density of the area elements is increased. The interpolation can significantly improve the smoothness of the image because the noise typically has a white Gaussian distribution with a zero mean. Moreover, interpolation can compensate for the roughness of the sparsely sampled phase space.

3.1.2 *Wavelet denoising*

The 2D matrix array is denoised using a BayesShrink-based wavelet threshold denoising algorithm [19], which tends to result in an overly smooth image compared to that obtained with a single threshold. The wavelet denoising algorithm consists of three steps: (1) applying the wavelet transform. This transformation decomposes the noisy image into different frequency sub-bands and generates a series of wavelet coefficients, (2) applying a thresholding method. There exist various algorithms estimating the threshold, such as VisuShrink, SureShrink, NormalShrink, and BayesShrink. The BayesShrink algorithm is an adaptive approach to wavelet soft thresholding where a unique threshold is estimated for each wavelet sub-band [19], which is more effective in removing Gaussian noise [20], and (3) reconstructing the image. By adopting the inverse wavelet transformation, the denoised image can be recovered.

3.1.3 *ROI selection*

The marching squares-based edge detection algorithm [21] is adopted to mask an ROI, which is the area containing only the good data. The marching squares algorithm is a special case of the marching cubes algorithm, which generates contours for a two-dimensional scalar field. In reality, a series of contour lines is generated, the number of which depends strongly on the contour level. Typically, it is desirable to select the biggest one as the ROI. The next step is to set the signal outside the ROI to zero and keep the inside, which will be further denoised, unchanged. While continuing to repeat the operation with an increased contour level, a curve can be generated that gives the trend of the emittance against the contour level. By fitting the smooth part of the curve with a line and extrapolating to the position at which the contour level is zero, the unbiased estimation of the emittance can be obtained. The remarkable advantage of this algorithm compared to the typical global denoising algorithms is the isolation of the major noise from the ROI, e.g., wire damage. In addition, the automatic selection of the ROI is also a significant improvement to the unbiased emittance evaluation.

A virtual simulated measurement is then taken, which is done to benchmark the proposed algorithm. In this simulation, the user-specified beam parameters as well as the associated noise distribution are given to generate the noisy beam. A virtual slit with an adjustable opening samples the beamlet, and a grid downstream collects the particle hits on the wire. The simulation parameters used are summarized in Table 2, where Q_len is the quadrupole length and D is the drift length. Figure 3 shows the noisy and reconstructed phase space. It is obvious that the signal-to-noise ratio is significantly improved after interpolation, wavelet denoising, and ROI selection have been implemented. The measured 1 σ ellipse matches the actual version well except that the tail is shorter than expected, which can be explained by the long tail of the Gaussian distribution being smeared by the noise and then cut out by the threshold. The obtained emittance as a function of threshold is shown in the upper panel of Fig. 4. A linear fit is applied to the region that has a constant derivative, and extrapolation is performed to obtain the "real" emittance with a zero threshold. The measured emittance is consistent with the specified value. The quantized error decreases with the increased interpolation number as shown in the lower panel of Fig. 4, and a deviation of below 4% is reached when interpolation number 4 is given.

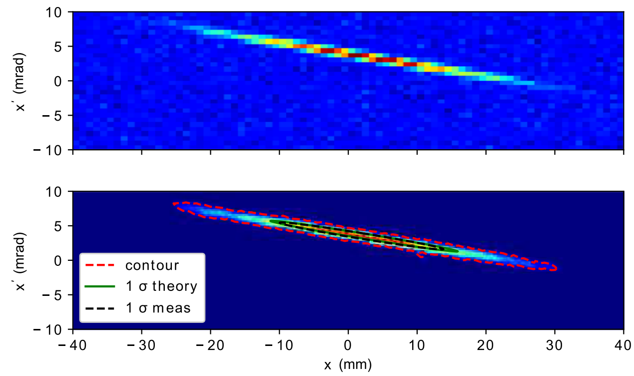

Fig. 3 Reconstructed phase space using the beam parameters listed in Table 1 with a slit gap of 1 mm, a slit step of 1 mm, a wire gap of 1 mm, a wire diameter of 0.1 mm, and a drift length of 1.5 m. Upper panel: noisy distribution; lower panel: denoised and marked phase space

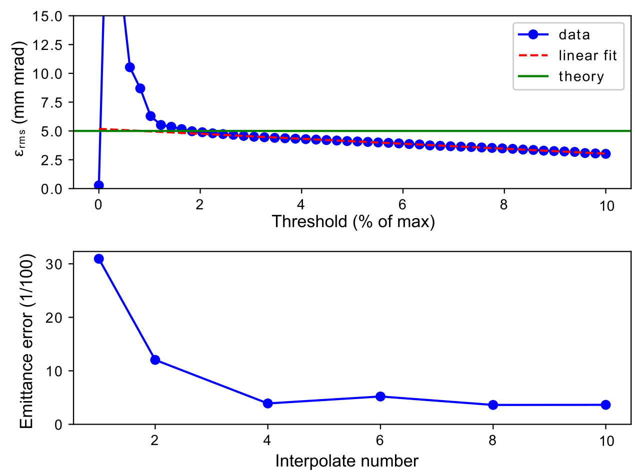

Fig. 4 Upper panel: the emittance evolution against the threshold; lower panel: the error of the reconstructed emittance against the interpolation number

In this measurement scheme, SL1&SL2, SL3&SL4, and MW4 are employed to perform measurements of the horizontal and vertical planes. The distance between the slit and the MW is 2.8295 m and 2.6692 m for the horizontal and vertical planes, respectively, which results in an angle resolution of 0.353 mrad and 0.375 mrad, respectively, based on the definition $\Delta x' = (d_{\mathrm{wire}} + 2r_{\mathrm{wire}})/L$, where d_{wire} is the gap between the wires, r_{wire} is the diameter of the wire, and L is the distance. The aperture of the slit for both of the planes is set to 1 mm, which is identical to the MW spacing, and the slit stepping length is also 1 mm, so the whole phase plane can be scanned without overlapping.

The raw data are averaged over the whole sample length to cancel the random noise preliminarily. The initial and denoised phase spaces are shown in the upper panels of Figs. 5 and 6 for the horizontal and vertical planes, respectively. A significant difference is observed when the denoising procedure described above is implemented. The contour line defines the beam boundary precisely. The

Table 2 Simulation parameters

Parameter	ϵ_{rms} (μm)	β (m)	α (rad)	E_{k} (MeV/u)	Ion	Q_{len} (m)	D (m)
Value	5	37	6	0.26	$^{12}C^{6+}$	0.4	2.38

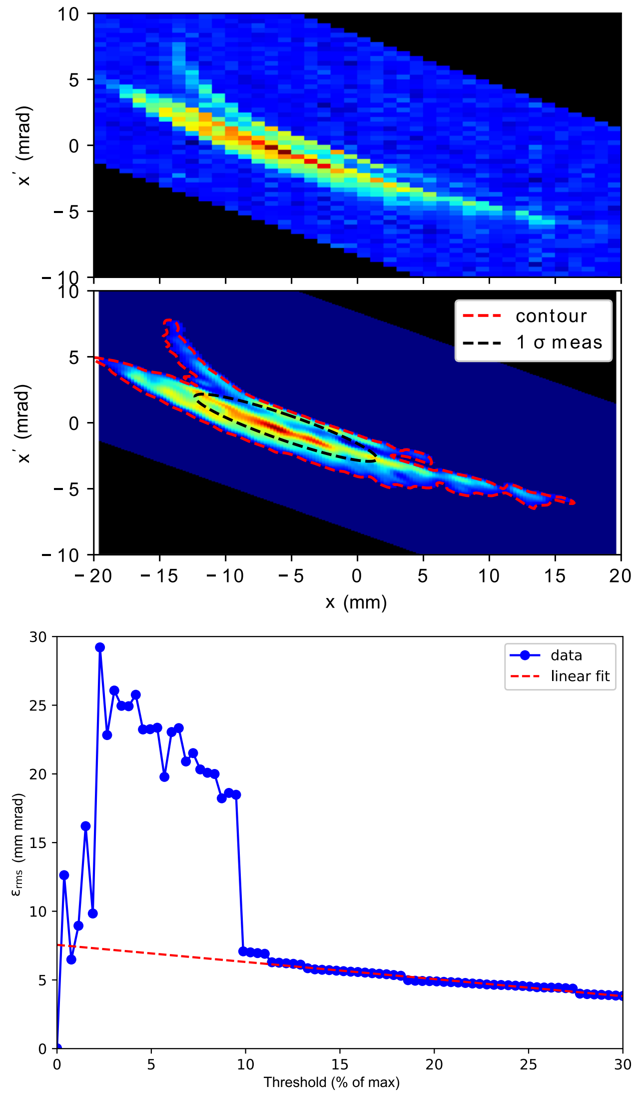

Fig. 5 Horizontal phase space and emittance evaluation. Upper panel: the raw phase space (top) and the denoised phase space (bottom). The red dashed line is the contour line with a contour level of 10%, and the black dashed line is the measured 1σ phase ellipse. Lower panel: the emittance evolution under the various contour levels (Color online)

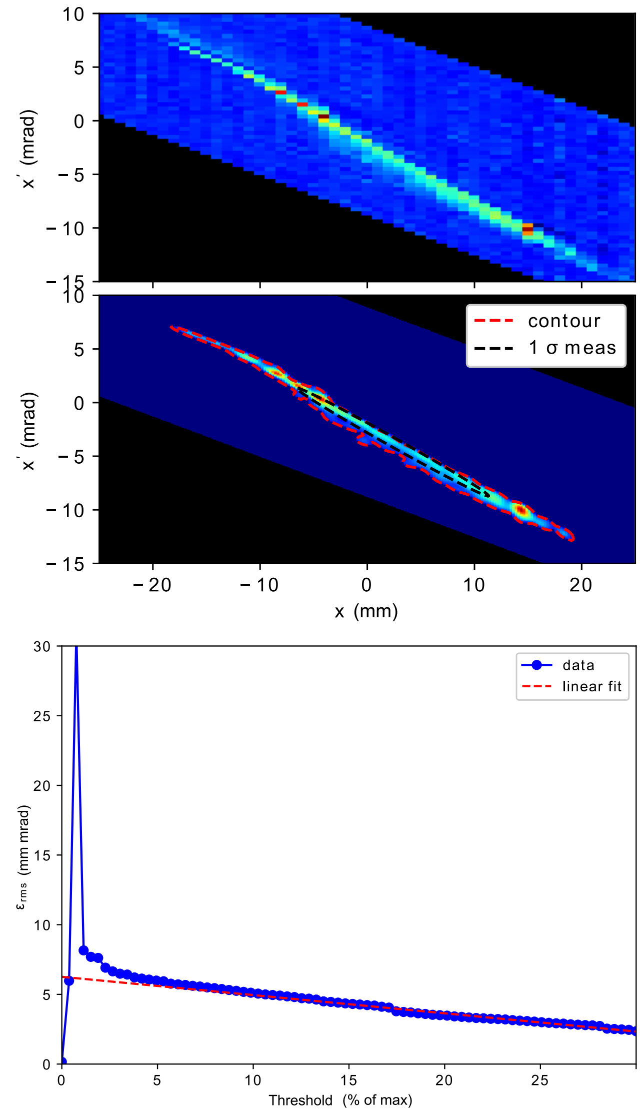

Fig. 6 Vertical phase space and emittance evaluation. Upper panel: the raw phase space (top) and the denoised phase space (bottom). The red dashed line is the contour line with a contour level of 15%, and the black dashed line is the measured 1σ phase ellipse. Lower panel: the emittance evolution under the various contour levels (Color online)

measured 95% emittance is 45.32 mm mrad and 37.56 mm mrad for the horizontal and vertical planes, respectively.

3.2 Q-scan technique

For a beam line with low intensity, like the diagnostics line of the HIMM cyclotron, the space-charge effects can be negligible; hence, the Q-scan technique is suitable for emittance measurements. If the focus length of the lens is larger than the length of the lens itself, a thin lens approximation can be adopted. The most frequently used case is a quadrupole followed by a drift section. Thus, the squared profile width at the MW is a quadratic function of the quadrupole gradient. Quite often, for a thin lens approximation, the thick lens is assumed to have zero length while keeping the strength constant. In this paper, we introduce a new method to split the thick lens into one thin lens plus two drift sections, which is the first-order approximation of the thick lens, and the conjugate of the three elements satisfies the symplectic condition. The schematic is shown in Fig. 7.

Without the loss of generality, the transfer matrix of a thick lens can be expressed as

$$\boldsymbol{M}_{\text{thick}} = \begin{bmatrix} C & S \\ C' & S' \end{bmatrix} \tag{3}$$

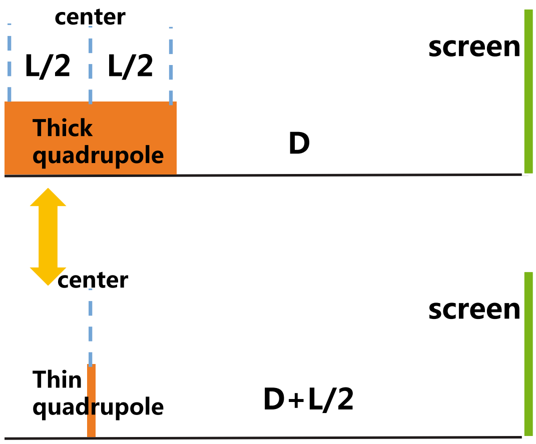

Fig. 7 Thick lens split

According to the split method mentioned above, the matrix can thus be written equivalently as $\boldsymbol{M}_{\text{thick}} = \boldsymbol{M}_{\text{drift1}}\boldsymbol{M}_{\text{thin}}\boldsymbol{M}_{\text{drift2}}$, where

$$\boldsymbol{M}_{\text{drift1}} = \begin{bmatrix} 1 & L_1 \\ 0 & 1 \end{bmatrix}$$
$$\boldsymbol{M}_{\text{thin}} = \begin{bmatrix} 1 & 0 \\ -K & 1 \end{bmatrix} \tag{4}$$
$$\boldsymbol{M}_{\text{drift2}} = \begin{bmatrix} 1 & L_2 \\ 0 & 1 \end{bmatrix}$$

If we assume $L_1 = L_2 = L/2$, the following equation will be obtained

$$K = -C', \quad \frac{L}{2} = \frac{C-1}{C'} \tag{5}$$

The evolution of $L/2$ with respect to quadrupole strength is illustrated in Fig. 8. Since the change of the half-length with quadrupole current is sufficiently small, the average over the scan current gives a better substitution. Therefore, the effective drift length now becomes $\langle L/2 \rangle + D$ with D being the original distance from the quadrupole exit to the MW. Evidently, this split method represents the thick lens more reliably.

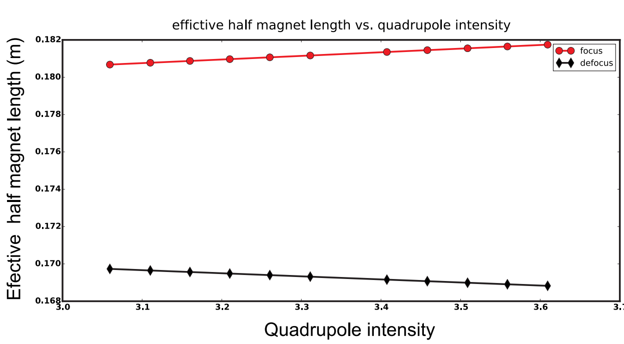

Fig. 8 Change of the effective magnet versus the quadrupole current

The actual energy is measured based on three phase probes along the beam line, and this gives the measurement value of 6.323 MeV/u, which is slightly different from the theoretical value. The magnet calibration curve is given by $B' = 0.01347 + 0.0219 I_{\text{Q}}$, where I_{Q} is the quadrupole current. The quadrupole length is 0.35 m; thus, the quadrupole strength can be calculated by $K = |\frac{B'}{B\rho}|L$ with $B\rho = 0.871$ Tm. The profile data for each step of the quadrupole-scan are averaged over the sample length, and a parabolic fit is performed. The algorithm is identical to that in Ref. [22]. The measurement data and fit process are shown in Fig. 9. The measured 95% emittance is 51.5 mm mrad and 31.8 mm mrad for the horizontal and vertical planes, respectively.

3.3 3-Grid technique

In this measurement, MW1, MW2, and MW3 are used to sample the profile. The emittance can thus be retrieved

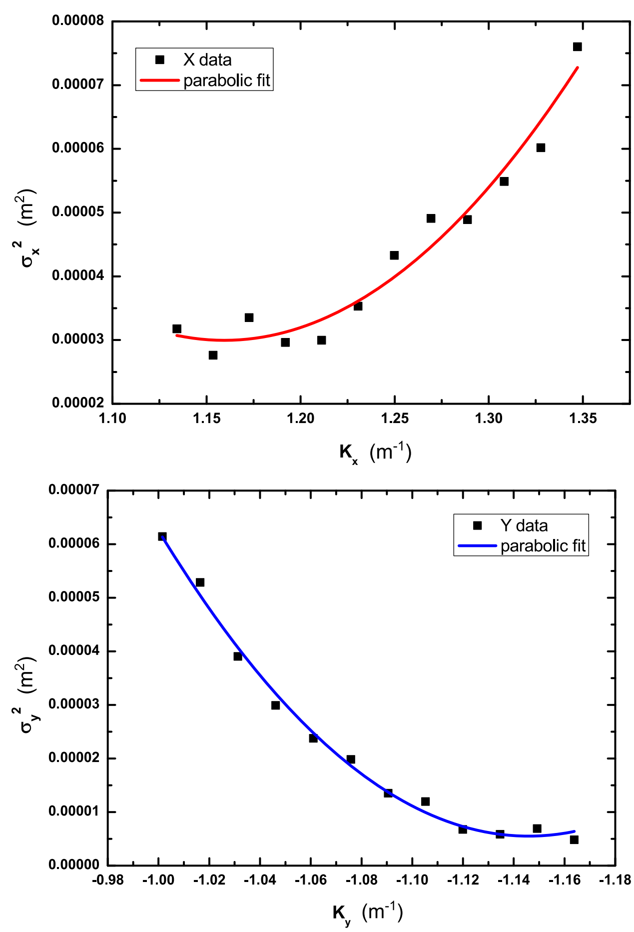

Fig. 9 Q-scan data and parabolic fit. Upper panel: the horizontal plane; lower panel: the vertical plane (Color online)

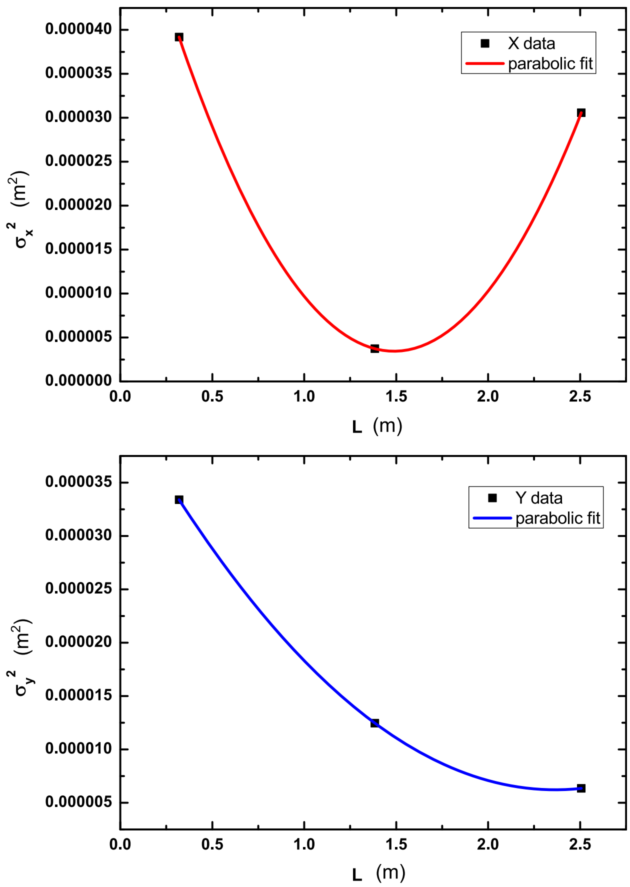

Fig. 10 3-grid data and parabolic fit. Upper panel: the horizontal plane; lower panel: the vertical plane (Color online)

uniquely by virtue of a parabolic fit or by solving the following linear equations directly.

$$\begin{bmatrix} \sigma_{11}(0) \\ \sigma_{12}(0) \\ \sigma_{22}(0) \end{bmatrix} = \begin{bmatrix} 1 & 2L_1 & L_1^2 \\ 1 & 2L_2 & L_2^2 \\ 1 & 2L_3 & L_3^2 \end{bmatrix}^{-1} \begin{bmatrix} \sigma_{11}(1) \\ \sigma_{11}(2) \\ \sigma_{11}(3) \end{bmatrix} \quad (6)$$

Both methods give the identical results as expected. The measurement data and fit process are shown in Fig. 10. The measured 95% emittance is 56.93 mm mrad and 38.15 mm mrad for the horizontal and vertical planes, respectively.

4 Summary

In this study, the emittance at the exit of the HIMM cyclotron was measured using three methods. The slit–grid algorithm was improved by introducing the automatic selection of an ROI, and a satisfactory result was obtained. For the Q-scan method, an optimized thin lens approximation algorithm was implemented, which gave a more reliable result. As presented in Table 3, the results of these measurements agree with one another for the vertical plane. There is a discrepancy for the horizontal plane, however. Based on our preliminary deductions, this is attributed to the nonzero dispersion contribution. The dispersion and its derivative are − 1.77 m and − 0.66 rad in the horizontal plane at the exit of cyclotron, respectively, and the temporal beam line is not designed to be dispersion-free in the diagnostics section.

Table 3 Measurement results

Methods	Slit–grid	Q-scan	3-Grid
Horizontal (95%) (mm mrad)	45.32	51.5	56.93
Vertical (95%) (mm mrad)	37.56	31.8	38.15

References

1. J. Yang, J. Shi, W. Chai et al., Design of a compact structure cancer therapy synchrotron. Nucl. Instrum. Methods Phys. Res. A **756**, 19–22 (2014). https://doi.org/10.1016/j.nima.2014.04.050
2. M. Li, S.P. Li, W.L. Li et al., The design and implementation of the beam diagnostics control system for HIMM. Nucl. Instrum. Methods Phys. Res. A **919**, 27–35 (2019). https://doi.org/10.1016/j.nima.2018.11.134
3. Y.C. Chen, Y.C. Feng, R.S. Mao et al., in *Optimization and Upgrade of Slow Extraction Control System for HIRFL CSR Main Ring*. ICALEPCS2017, Barcelona, Spain, p. 1663. https://doi.org/10.18429/JACoW-ICALEPCS2017-THPHA122
4. J. Shi, J.C. Yang, J.W. Xia et al., Heavy ion medical machine (HIMM) slow extraction commissioning. Nucl. Instrum. Methods Phys. Res. A **918**, 76–81 (2019). https://doi.org/10.1016/j.nima.2018.11.014
5. P.M. Lapostolle, Possible emittance increase through filamentation due to space charge in continuous beams. IEEE Trans. Nucl. Sci. **18**(3), 1101–1104 (1971). https://doi.org/10.1109/TNS.1971.4326292
6. C. Lejeune, J. Aubert, Emittance and brightness: definitions and measurements, in *Applied Charged Particle Optics*, vol. Part A, ed. by A. Septier (Academic Press, New York, 1980), p. 159
7. J. Montano, J. Vasquez, A. Andrighetto et al., Off-line emittance measurements of the SPES ion source at LNL. Nucl. Instrum. Methods Phys. Res. A **648**, 238–245 (2011). https://doi.org/10.1016/j.nima.2011.05.038
8. X.H. Wang, Z.G. He, J. Fang, Slit-based emittance measurement system for high-brightness injector at Hefei light source. High Power Laser Part. Beams **24**, 457–462 (2012). https://doi.org/10.3788/HPLPB20122402.0457. (in Chinese)
9. J.L. Ke, C.G. Zhou, R. Qiu, Transverse emittance measurement of high-current single pulse beams using pepper-pot method. High Power Laser Part. Beams **25**, 2067–2070 (2013). https://doi.org/10.3788/HPLPB20132508.2067. (in Chinese)
10. C. Thomas, N. Delerue, R. Bartolini, Single shot 3 GeV electron transverse emittance with a pepper-pot. Nucl. Instrum. Methods Phys. Res. A **729**, 554–556 (2013). https://doi.org/10.1016/j.nima.2013.07.017
11. T. Nagatomo, V. Tzoganis, M. Kase et al., Development of a pepper-pot emittance meter for diagnostics of low-energy multiply charged heavy ion beams extracted from an ECR ion source.

Rev. Sci. Instrum. **87**, 02B920 (2016). https://doi.org/10.1063/1.4934688

12. F. Lohl, S. Schreiber, M. Castellano et al., Measurements of the transverse emittance at the FLASH injector at DESY. Phys. Rev. Spec. Top. Accel. Beams **9**, 092802 (2006). https://doi.org/10.1103/PhysRevSTAB.9.092802
13. M. Olvegard, V. Ziemann, Effect of large momentum spread on emittance measurements. Nucl. Instrum. Methods Phys. Res. A **707**, 114–119 (2013). https://doi.org/10.1016/j.nima.2012.12.114
14. Z. Zhang, X.G. Jiang, Pulsed intense electron beam emittance measurement. Nucl. Sci. Tech. **25**, 060201 (2014). https://doi.org/10.13538/j.1001-8042/nst.25.060201
15. L.Y. Zhang, J.J. Zhuang, Calculation of two-screen emittance measurement. Nucl. Instrum. Methods Phys. Res. A **407**, 356–358 (1998). https://doi.org/10.1016/S0168-9002(98)00049-7
16. G. Michiko, *Minty, Frank Zimmermann, Measurement and Control of Charged Particle Beams* (Springer, Berlin, 2013), p. 99
17. M. Li, Y.J. Yuan, R.S. Mao et al., The control system of the multi-strip ionization chamber for the HIMM. Nucl. Instrum. Methods Phys. Res. A **776**, 21–26 (2015). https://doi.org/10.1016/j.nima.2014.12.021
18. A.W. Chao, K.H. Mess, M. Tigner, *Handbook of Accelerator Physics and Engineering*, 2nd edn. (World Scientific, Beijing, 2013), p. 704
19. G. Lee, R. Gommers, F. Wasilewski et al., *Pywavelets-wavelet transforms in python*. Accessed 19 Sep 2018 (2006). https://doi.org/10.5281/zenodo.1407172
20. S.G. Chang, B. Yu, M. Vetterli, Adaptive wavelet thresholding for image denoising and compression. IEEE Trans. Image Process. **9**(9), 1532–1546 (2000). https://doi.org/10.1109/83.862633
21. S. van der Walt, J.L. Schnberger, J. Nunez-Iglesias et al., scikit-image: image processing in python. PeerJ **2**, e453 (2014). https://doi.org/10.7717/peerj.453
22. P. Forck, *Lecture Notes on Beam Instrumentation and Diagnostics* (GSI, Darmstadt, 2011), p. 73